

Design and performance of a space–time virtual element method for the heat equation on prismatic meshes *

Sergio Gómez^{†‡}, Lorenzo Mascotto^{§¶}, Ilaria Perugia[¶]

Abstract

We present a space–time virtual element method for the discretization of the heat equation, which is defined on general prismatic meshes and variable degrees of accuracy. Strategies to handle efficiently the space–time mesh structure are discussed. We perform convergence tests for the h - and hp -versions of the method in case of smooth and singular solutions, and test space–time adaptive mesh refinements driven by a residual-type error indicator.

AMS subject classification: 35K05; 65N12; 65N30.

Keywords: virtual element methods; heat equation; space–time methods; polytopic meshes.

1 Introduction

Space–time Galerkin methods aim at approximating solutions to time-dependent partial differential equations discretizing the space and time variables at once. Even though the foundation of space–time Galerkin methods traces back to the 70ies of the last century [12] and a few contributions were developed in the twenty years to follow [2, 3, 6, 7, 11], only in the last two decades there has been a growing attention on this topic, mainly due to the improved performance of computers.

Compared to the time-stepping approach, space–time Galerkin methods have some important upsides and features: the discrete solution can be evaluated on the whole space–time domain and not only at a finite number of times; such methods allow for space–time adaptivity; it is possible to design space–time parallel solvers.

In this paper, we focus on the approximation of solutions to the heat equation. Several space–time methods have been designed to this aim and they can be classified into two main groups. The first one is based on the discretization of a standard Petrov-Galerkin formulation [5]; see [1, 18] for continuous finite element methods, [17] for a wavelet method, [4, 23] for discontinuous Galerkin methods, [13] for an isogeometric method, [21] for a coercive method based on a Hilbert transformation of the test space, and [22] for a mixed finite element method. Residual-type error indicators for the method of [18] were considered in [19, 20]. Possible drawbacks of employing continuous finite elements are that suboptimal convergence rates are obtained for some singular solutions, and incompatible boundary and initial conditions cannot be naturally handled.

The second group is based on first order system least squares discretizations (FOSLS); see [8, 9, 24] for finite element methods and [14] for isogeometric methods. Space–time FOSLS finite elements naturally provide reliable and efficient error indicators; see [8, 9, 15]. However, they require the computation of an additional vector-valued flux variable.

In this paper, we extend the nonconforming space–time virtual element method of [10] to the case of general prismatic meshes and nonuniform degrees of accuracy. This method allows for the

*The authors have been funded by the Austrian Science Fund (FWF) through the projects F 65 and P 33477 (I. Perugia), and the Italian Ministry of University and Research through the PRIN project “NA-FROM-PDEs” and PNRR-M4C2-I1.4-NC-HPC-Spoke6 (S. Gómez). S. Gómez acknowledges the kind hospitality of the Erwin Schrödinger International Institute for Mathematics and Physics (ESI), where part of this research was developed.

[†]Department of Mathematics, University of Pavia, 27100 Pavia, Italy (sergio.gomez01@universitadipavia.it)

[‡]Erwin Schrödinger Institute for Mathematics and Physics, University of Vienna, Austria

[§]Department of Mathematics and Applications, University of Milano-Bicocca, 20125 Milan, Italy (lorenzo.mascotto@unimib.it)

[¶]Faculty of Mathematics, University of Vienna, 1090 Vienna, Austria (ilaria.perugia@univie.ac.at)

^{||}IMATI-CNR, Pavia, Italy

use of space–time meshes with hanging facets (nodes, edges, faces) and is based on discontinuous in time test and trial functions that are solutions to local space–time problems with polynomial data. This approach provides a natural framework for space–time adaptivity without need of remeshing neighbouring elements. If the space–time mesh is decomposed into separate time-slabs, the global linear system can be split into much smaller systems that can be solved sequentially. Due to the nonconformity across time-like facets, the design and implementation of the method are independent of the spatial dimension. No artificial compatibility of initial and boundary conditions is enforced on the trial virtual element space, and optimal convergence rates have been achieved also for singular solutions. However, the stability analysis of the method relies on a discrete inf-sup condition and the method requires a stabilization term for the spatial Laplacian that needs to be carefully designed; see [10].

The main goals of this manuscript are:

- to construct a space–time virtual element method on general prismatic meshes, possibly with hanging facets and variable degrees of accuracy;
- to discuss suitable strategies to handle efficiently the space–time mesh structure;
- to investigate h - and hp - refinements numerically;
- to test space–time adaptive mesh refinements driven by a residual-type error indicator.

In the remainder of this section, we introduce some notation and the model problem. Finally, we outline the structure of the paper.

1.1 Notation

We denote the first partial derivative with respect to the time variable t by ∂_t , and the spatial gradient and Laplacian operators by $\nabla_{\mathbf{x}}$, $\Delta_{\mathbf{x}}$, respectively.

Standard notation for Sobolev spaces is employed. For a given domain D in \mathbb{R}^d , $d \in \mathbb{N}$, $H^s(D)$ represents the standard Sobolev space of order s in \mathbb{N} endowed with the standard inner product $(\cdot, \cdot)_{s,D}$, the seminorm $|\cdot|_{s,D}$, and the norm $\|\cdot\|_{s,D}$. In particular, we let $H^0(D)$ be the space $L^2(D)$ of Lebesgue square integrable functions over D and $H_0^1(D)$ be the subspace of functions in $H^1(D)$ with zero trace on ∂D . If s is a fractional or negative number, then the Sobolev space $H^s(D)$ is defined by means of interpolation and duality, respectively. We denote the duality product between $H^{-1}(D)$ and $H_0^1(D)$ by $\langle \cdot, \cdot \rangle$. The Sobolev spaces on ∂D are defined analogously and denoted by $H^s(\partial D)$.

Given s in \mathbb{R} , a time interval (a, b) , and a Banach space $(Z, \|\cdot\|_Z)$, we introduce the Bochner space $H^s(a, b; Z)$. In particular, we define

$$Y := L^2(0, T; H_0^1(\Omega)), \quad X := \{v \in Y \cap H^1(0, T; H^{-1}(\Omega)) \mid v(\mathbf{x}, 0) = 0 \forall \mathbf{x} \in \Omega\}. \quad (1)$$

We endow Y and X with the norms

$$\|v\|_Y^2 := \int_0^T |v(\cdot, t)|_{1,\Omega}^2 dt, \quad \|v\|_X^2 := c_H \|\partial_t v\|_{L^2(0,T;H^{-1}(\Omega))}^2 + \|v\|_Y^2, \quad (2)$$

respectively, where we have set

$$\|\phi\|_{L^2(0,T;H^{-1}(\Omega))} := \sup_{0 \neq v \in Y} \frac{\int_0^T \langle \phi, v \rangle dt}{\|v\|_Y}.$$

We denote the space of polynomials in d variables of degree at most p on a domain $D \subset \mathbb{R}^d$ by $\mathbb{P}_p(D)$.

1.2 Model problem

We consider the heat equation on the space–time domain $Q_T := \Omega \times (0, T)$, where $\Omega \subset \mathbb{R}^d$, $d = 1, 2, 3$, and $T > 0$ are the (bounded) spatial domain and the final time, respectively.

Associated with Q_T , we introduce the space-like surface $\Sigma_0 := \Omega \times \{0\}$ and the time-like surface $\Sigma_D := \partial\Omega \times (0, T)$.

Let $f : Q_T \rightarrow \mathbb{R}$, $u_0 : \Sigma_0 \rightarrow \mathbb{R}$, and $g : \Sigma_D \rightarrow \mathbb{R}$ denote the source term, initial condition, and Dirichlet boundary condition, respectively. We assume $f \in L^2(0, T; H^{-1}(\Omega))$. We further consider $c_H > 0$ and $\nu > 0$ given positive constant volumetric heat capacity and thermal conductivity, respectively.

The heat equation in strong formulation reads: find a function $u : Q_T \rightarrow \mathbb{R}$ such that

$$\begin{cases} c_H \partial_t u - \nu \Delta_{\mathbf{x}} u = f & \text{in } Q_T, \\ u = u_0 & \text{on } \Sigma_0, \\ u = g & \text{on } \Sigma_D. \end{cases} \quad (3)$$

To simplify the presentation, we henceforth assume that $u_0 = 0$ and $g = 0$. Nonetheless, in Sections 4 and 5, we present numerical results for solutions with inhomogeneous initial and boundary conditions.

Define the space–time bilinear form $b(\cdot, \cdot) : X \times Y \rightarrow \mathbb{R}$ as

$$b(u, v) := \int_0^T \langle c_H \partial_t u, v \rangle dt + \int_0^T \int_{\Omega} \nu \nabla_{\mathbf{x}} u \cdot \nabla_{\mathbf{x}} v \, dx dt. \quad (4)$$

We consider the Petrov-Galerkin weak formulation of (3) as in [5]:

$$\begin{cases} \text{find } u \in X \text{ such that} \\ b(u, v) = \int_0^T \langle f, v \rangle dt \quad \forall v \in Y. \end{cases} \quad (5)$$

Problem (5) is well posed; see, e.g., [18, Corollary 2.3].

Structure of the paper. In Section 2, we design a space–time virtual element method for the approximation of solutions to (5) on general prismatic meshes; in Section 3, strategies to handle efficiently the space–time mesh structure are discussed, including flagging strategies that might be used for other polytopic methods as well; in Section 4, we assess the convergence of the h - and hp -versions of the method on some singular solutions; in Section 5, a computable residual-type error indicator is defined and used to lead adaptive mesh refinements.

2 The space–time virtual element method

We describe a nonconforming space–time virtual element method for the approximation of solutions to (5). We proceed in several steps: we introduce general prismatic meshes in Section 2.1; design local virtual element spaces and describe their degrees of freedom (DoFs) in Section 2.2; show that the choice of the DoFs allows for the computation of orthogonal projectors onto polynomial spaces in Section 2.3; define global nonconforming space–time virtual element spaces in Section 2.4; detail the discrete bilinear forms in Section 2.5; present the method in Section 2.6.

2.1 General prismatic meshes

We consider sequences of meshes $\{\mathcal{T}_h\}$ consisting of nonoverlapping prismatic-type polytopes covering Q_T in the following sense: each element K in \mathcal{T}_h shares its volume with a prism \mathcal{K} given by the tensor product of an open d -polytopic “spatial” basis $\mathcal{K}_{\mathbf{x}}$ with boundary $\partial\mathcal{K}_{\mathbf{x}}$ and a “time” interval $\mathcal{K}_t := (a_t, b_t)$. We denote the diameter of $\mathcal{K}_{\mathbf{x}}$ and the length of \mathcal{K}_t by $h_{\mathcal{K}_{\mathbf{x}}}$ and $h_{\mathcal{K}_t}$, respectively.

For each element K , we distinguish two types of nonoverlapping d -dimensional polytopic facets: space-like facets $K_{\mathbf{x}}$, whose union gives $\mathcal{K}_{\mathbf{x}} \times \{a_t\}$, and time-like facets $F := F_{\mathbf{x}} \times F_t$, where $F_{\mathbf{x}} \subset$

$\partial\mathcal{K}_{\mathbf{x}}$ is a facet of some $K_{\mathbf{x}}$ and $F_t \subset \mathcal{K}_t$.¹ We collect the space-like and time-like facets of K into the sets $\mathcal{F}_K^{\text{space}}$ and $\mathcal{F}_K^{\text{time}}$. For any $F_{\mathbf{x}} \in \mathcal{F}_K^{\text{space}}$, we define

$$h_{F_{\mathbf{x}}} := \begin{cases} \min\{h_{K_{\mathbf{x}}}, h_{\tilde{K}_{\mathbf{x}}}\} & \text{if } F_{\mathbf{x}} = K_{\mathbf{x}} \cap \tilde{K}_{\mathbf{x}} \text{ with } \tilde{K}_{\mathbf{x}} \in \mathcal{F}_{\tilde{K}}^{\text{space}} \text{ for some } \tilde{K} \in \mathcal{T}_h, \\ h_{K_{\mathbf{x}}} & \text{if } F_{\mathbf{x}} \subset \partial\Omega. \end{cases}$$

We define the sets of *space-like* and *time-like* facets of \mathcal{T}_h as

$$\mathcal{F}_h^{\text{space}} := \bigcup_{K \in \mathcal{T}_h} \mathcal{F}_K^{\text{space}}, \quad \mathcal{F}_h^{\text{time}} := \bigcup_{K \in \mathcal{T}_h} \mathcal{F}_K^{\text{time}}.$$

Hanging nodes (1+1 dimensional case), edges (2+1 dimensional case), and faces (3+1 dimensional case) are automatically included within this structure of the mesh. For each F in $\mathcal{F}_h^{\text{time}}$, we fix a normal unit vector \mathbf{n}_F in \mathbb{R}^{d+1} of the form $(\mathbf{n}_{F_{\mathbf{x}}}, 0)$, $\mathbf{n}_{F_{\mathbf{x}}} \in \mathbb{R}^d$.

For a given mesh \mathcal{T}_h , we define the broken Sobolev space of order $s \in \mathbb{R}^+$ as

$$H^s(\mathcal{T}_h) := \{v \in L^2(\Omega) \mid v|_K \in H^s(K) \forall K \in \mathcal{T}_h\},$$

and endow it with the standard broken norm $\|\cdot\|_{s, \mathcal{T}_h}$ and seminorm $|\cdot|_{s, \mathcal{T}_h}$. We denote the space of piecewise polynomials of maximum degree $p \in \mathbb{N}$ over \mathcal{T}_h by $\mathcal{S}_p(\mathcal{T}_h)$.

2.2 Local space–time virtual element spaces

We introduce local space–time virtual element spaces, extending the construction in [10] to more general meshes as in Section 2.1.

Introduce the scaling factors

$$\tilde{c}_H^K := h_{\mathcal{K}_t}, \quad \tilde{v}^K := h_{\mathcal{K}_{\mathbf{x}}}^2. \quad (6)$$

Given p in \mathbb{N} and K an element in \mathcal{T}_h , we define the local space–time virtual element space as

$$V_h(K) := \left\{ v \in L^2(K) \mid \tilde{c}_H^K \partial_t v_h - \tilde{v}^K \Delta_{\mathbf{x}} v_h \in \mathbb{P}_{p-1}(K); \right. \\ \left. v_h|_{\mathcal{K}_{\mathbf{x}}} \in \mathbb{P}_p(\mathcal{K}_{\mathbf{x}}); \mathbf{n}_{F_{\mathbf{x}}} \cdot \nabla_{\mathbf{x}} v_h|_F \in \mathbb{P}_p(F) \forall F \in \mathcal{F}_K^{\text{time}} \right\}. \quad (7)$$

Functions in $V_h(K)$ are not known in closed form. Yet, $\mathbb{P}_p(K)$ is contained in $V_h(K)$.

Given an element K and any of its time-like facets F , let $\{m_{\alpha}^K\}_{\alpha=1}^{\dim(\mathbb{P}_{p-1}(K))}$, $\{m_{\beta}^F\}_{\beta=1}^{\dim(\mathbb{P}_p(F))}$, and $\{m_{\gamma}^{\mathcal{K}_{\mathbf{x}}}\}_{\gamma=1}^{\dim(\mathbb{P}_p(\mathcal{K}_{\mathbf{x}}))}$ be given bases of $\mathbb{P}_{p-1}(K)$, $\mathbb{P}_p(F)$, and $\mathbb{P}_p(\mathcal{K}_{\mathbf{x}})$, respectively. Those basis elements are assumed to be invariant with respect to translations and dilations.

Introduce the following set of linear functionals:

- the *bulk* moments

$$\frac{1}{|K|} \int_K v_h m_{\alpha}^K \, d\mathbf{x} \, dt, \quad \alpha = 1, \dots, \dim(\mathbb{P}_{p-1}(K)); \quad (8)$$

- for all *time-like* facets $F \in \mathcal{F}_K^{\text{time}}$, the *time-like* moments

$$\frac{1}{|F|} \int_F v_h m_{\beta}^F \, dS \, dt, \quad \beta = 1, \dots, \dim(\mathbb{P}_p(F)); \quad (9)$$

- the *space-like* moments

$$\frac{1}{|\mathcal{K}_{\mathbf{x}}|} \int_{\mathcal{K}_{\mathbf{x}}} v_h(\cdot, t_{n-1}) m_{\gamma}^{\mathcal{K}_{\mathbf{x}}} \, d\mathbf{x}, \quad \gamma = 1, \dots, \dim(\mathbb{P}_p(\mathcal{K}_{\mathbf{x}})). \quad (10)$$

These linear functionals constitute a set of unisolvent degrees of freedom for the space $V_h(K)$. To see this, it suffices to extend [10, Lemma 2.1] to the case of the general prismatic-type elements introduced in Section 2.1.

¹We do not need to classify facet(s) of K on $\mathcal{K}_{\mathbf{x}} \times \{b_t\}$. One may consider that the facet $\mathcal{K}_{\mathbf{x}} \times \{b_t\}$ is a unique (unclassified) facet of K .

2.3 Polynomial projections

Recall that each element K shares its volume with a prism \mathcal{K} given by $\mathcal{K}_{\mathbf{x}} \times \mathcal{K}_t$; see Section 2.1. We define four orthogonal projectors onto polynomial spaces: for all elements K and all $\varepsilon > 0$,

1. we introduce $\Pi_p^N : H^{\frac{1}{2}+\varepsilon}(\mathcal{K}_t; L^2(\mathcal{K}_{\mathbf{x}})) \cap L^2(\mathcal{K}_t; H^1(\mathcal{K}_{\mathbf{x}})) \rightarrow \mathbb{P}_p(K)$ as

$$\int_{\mathcal{K}_t} \int_{\mathcal{K}_{\mathbf{x}}} \nabla_{\mathbf{x}} q_p^K \cdot \nabla_{\mathbf{x}} (\Pi_p^N v - v) \, d\mathbf{x} dt = 0 \quad \forall q_p^K \in \mathbb{P}_p(K) \setminus \mathbb{P}_p(\mathcal{K}_t), \quad (11a)$$

$$\int_{\mathcal{K}_t} \int_{\mathcal{K}_{\mathbf{x}}} q_{p-1}(t) (\Pi_p^N v - v) \, d\mathbf{x} dt = 0 \quad \forall q_{p-1} \in \mathbb{P}_{p-1}(\mathcal{K}_t), \quad (11b)$$

$$\int_{\mathcal{K}_{\mathbf{x}}} (\Pi_p^N v(\mathbf{x}, t_{n-1}) - v(\mathbf{x}, t_{n-1})) \, d\mathbf{x} = 0; \quad (11c)$$

2. we introduce $\Pi_p^* : H^{\frac{1}{2}+\varepsilon}(\mathcal{K}_t; L^2(\mathcal{K}_{\mathbf{x}})) \rightarrow \mathbb{P}_p(K)$ as

$$\int_{\mathcal{K}_t} \int_{\mathcal{K}_{\mathbf{x}}} q_{p-1}^K (\Pi_p^* v - v) \, d\mathbf{x} dt = 0 \quad \forall q_{p-1}^K \in \mathbb{P}_{p-1}(K), \quad (12a)$$

$$\int_{\mathcal{K}_{\mathbf{x}}} q_p^{\mathcal{K}_{\mathbf{x}}} (\Pi_p^* v(\mathbf{x}, t_{n-1}) - v(\mathbf{x}, t_{n-1})) \, d\mathbf{x} = 0 \quad \forall q_p^{\mathcal{K}_{\mathbf{x}}} \in \mathbb{P}_p(\mathcal{K}_{\mathbf{x}}); \quad (12b)$$

3. we introduce $\Pi_{p-1}^{0,K} : L^2(K) \rightarrow \mathbb{P}_{p-1}(K)$ as

$$(q_{p-1}^K, v - \Pi_{p-1}^{0,K} v)_{0,K} = 0 \quad \forall q_{p-1}^K \in \mathbb{P}_{p-1}(K); \quad (13)$$

4. for all *time-like* facets F in $\mathcal{F}_K^{\text{time}}$, we introduce $\Pi_p^{0,F} : L^2(F) \rightarrow \mathbb{P}_p(F)$ as

$$(q_p^F, v - \Pi_p^{0,F} v)_{0,F} = 0 \quad \forall q_p^F \in \mathbb{P}_p(F). \quad (14)$$

Let v be a function in $V_h(K)$ with given degrees of freedom (8)–(10). Then, the proof of the well posedness and computability of the above four projectors follows by extending the results in [10, Section 2.2] to the case of general prismatic-type elements as in Section 2.1.

2.4 Global nonconforming space–time virtual element spaces

We design a global virtual element space Y_h , consisting of functions that are discontinuous in time and nonconforming in space.

To this aim, we introduce the jump operator on each time-like facet F as the functional $[[v]]_F : L^2(F) \rightarrow [L^2(F)]^{d+1}$ given by

$$[[v]]_F := \begin{cases} v|_{K_1} \mathbf{n}_{K_1}^F + v|_{K_2} \mathbf{n}_{K_2}^F & \text{if } F \subset \partial K_1 \cap \partial K_2 \text{ is an internal facet, } K_1, K_2 \in \mathcal{T}_h \\ v|_{K_3} \mathbf{n}_{K_3}^F & \text{if } F \subset \partial K_3 \text{ is a boundary facet, } K_3 \in \mathcal{T}_h. \end{cases}$$

Recall that any element K shares its volume with a prism $\mathcal{K} = \mathcal{K}_{\mathbf{x}} \times \mathcal{K}_t$; see Section 2.1. We define the Sobolev nonconforming space of order p associated with the mesh \mathcal{T}_h as

$$\mathcal{NC}_p(\mathcal{T}_h) := \left\{ v \in L^2(Q_T) \mid v|_K \in L^2(\mathcal{K}_t, H^1(\mathcal{K}_{\mathbf{x}})) \, \forall K \in \mathcal{T}_h; \right. \\ \left. \int_F q_p^F [[v]]_F \cdot \mathbf{n}_F \, dS = 0 \quad \forall q_p^F \in \mathbb{P}_p(F), \, \forall F \in \mathcal{F}_h^{\text{time}} \right\}. \quad (15)$$

We define the global virtual element space as follows:

$$Y_h := \left\{ v_h \in L^2(Q_T) \mid v_h|_K \in V_h(K) \, \forall K \in \mathcal{T}_h; \, v_h \in \mathcal{NC}_p(\mathcal{T}_h) \right\}.$$

2.5 The discrete bilinear forms

Since functions in the space–time virtual element space Y_h are not available in closed form, we discretize the bilinear forms by computable counterparts. On each element K , define the local continuous bilinear form and the induced norm

$$a^K(u_h, v_h) := \nu(\nabla_{\mathbf{x}} u_h, \nabla_{\mathbf{x}} v_h)_{0,K}, \quad |v_h|_{Y(K)}^2 := a^K(v_h, v_h) = \nu \|\nabla_{\mathbf{x}} v_h\|_{0,K}^2.$$

Let $S^K : V_h(K) \times V_h(K) \rightarrow \mathbb{R}$ be any symmetric bilinear form, which is computable via the degrees of freedom and satisfies the following property: there exist $0 < c_* < c^*$ independent of K such that

$$c_* |v_h|_{Y(K)}^2 \leq \nu S^K(v_h, v_h) \leq c^* |v_h|_{Y(K)}^2 \quad \forall v_h \in V_h(K) \cap \ker(\Pi_p^N). \quad (16)$$

Define

$$a_h^K(u_h, v_h) := a^K(\Pi_p^N u_h, \Pi_p^N v_h) + \nu S^K((I - \Pi_p^N)u_h, (I - \Pi_p^N)v_h). \quad (17)$$

Extending [10, Lemma 2.7] to the case of general prismatic-type elements as in Section 2.1, it is possible to prove that there exist $0 < \alpha_* < \alpha^*$ independent of K such that the following local stability bounds are valid:

$$\alpha_* |v_h|_{Y(K)}^2 \leq a_h^K(v_h, v_h) \leq \alpha^* |v_h|_{Y(K)}^2 \quad \forall v_h \in V_h(K). \quad (18)$$

Besides, we introduce upwind-type terms, which allows for imposing weakly the continuity in time of the trial functions: for all space-like facets $K_{\mathbf{x}} \subset \Omega \times \{t^*\}$, $t^* \in [0, T]$,

$$\mathcal{U}^{K_{\mathbf{x}}}(u_h) := \begin{cases} c_H \Pi_p^* u_h|_{K}(\cdot, t^*) & \text{if } t^* = 0 \\ c_H (\Pi_p^* u_h|_{K^+}(\cdot, t^*) - \Pi_p^* u_h|_{K^-}(\cdot, t^*)) & \text{if } t^* > 0, \end{cases} \quad (19)$$

where $K_{\mathbf{x}} \in \mathcal{F}_K^{\text{space}}$ if $t^* = 0$, and $K_{\mathbf{x}} \in F_{K^+}^{\text{space}}$ is a subset of $\partial K^+ \cap \partial K^-$ if $t^* > 0$.

Remark 1. The case of nonzero initial conditions can be dealt with by modifying the definition of the upwind functional at time $t = 0$ as follows: for all space-like facets $K_{\mathbf{x}} \subset \Omega \times \{0\}$,

$$\mathcal{U}^{K_{\mathbf{x}}}(u_h) := c_H (\Pi_p^* u_h|_{K}(\cdot, 0) - u_0).$$

■

The computability of the upwind terms follows from the definition of the space-like moment degrees of freedom (10) and the computability of the projector Π_p^* .

We define a discrete counterpart of the bilinear form $b(\cdot, \cdot)$ in (4) as follows:

$$b_h(u_h, v_h) := \sum_{K \in \mathcal{T}_h} [c_H (\partial_t \Pi_p^* u_h, v_h)_{0,K} + a_h^K(u_h, v_h)] + \sum_{K_{\mathbf{x}} \in \mathcal{F}_h^{\text{space}}} (\mathcal{U}^{K_{\mathbf{x}}}(u_h), v_h|_{K^+})_{0, K_{\mathbf{x}}}. \quad (20)$$

A computable stabilization satisfying (18) is given by

$$S^K(u_h, v_h) := p^2 h_{\mathcal{K}_{\mathbf{x}}}^{-2} (\Pi_{p-1}^{0,K} u_h, \Pi_{p-1}^{0,K} v_h)_{0,K} + \sum_{F \in \mathcal{F}_K^{\text{time}}} p h_{F_{\mathbf{x}}}^{-1} (\Pi_p^{0,F} u_h, \Pi_p^{0,F} v_h)_{0,F} + p h_{\mathcal{K}_t} h_{\mathcal{K}_{\mathbf{x}}}^{-2} (u_h, v_h)_{0, \mathcal{K}_{\mathbf{x}}}. \quad (21)$$

2.6 The method

Henceforth, we assume that f belongs to $L^2(Q_T)$. The space–time virtual element method for the approximation of solutions to (5) reads

$$\begin{cases} \text{find } u_h \in Y_h \text{ such that} \\ b_h(u_h, v_h) = (f, \Pi_{p-1}^0 v_h)_{0,\Omega} \quad \forall v_h \in Y_h. \end{cases} \quad (22)$$

For Cartesian-product-in-time meshes, the well posedness of the method and *a priori* error estimates were proven in [10, Sections 3 and 4] based on a discrete inf-sup argument. That analysis can be extended to the meshes introduced in Section 2.1, using the norms

$$\begin{aligned} \|v\|_{Y(\mathcal{T}_h)}^2 &:= \sum_{K \in \mathcal{T}_h} \|v\|_{Y(K)}^2, \\ \|v\|_{X(\mathcal{T}_h)}^2 &:= \|v\|_{Y(\mathcal{T}_h)}^2 + \|\mathfrak{N}_h \Pi_p^* v\|_{Y(\mathcal{T}_h)}^2 \\ &\quad + \frac{c_H}{2} \left(\|\Pi_p^* v(\cdot, 0)\|_{0,\Omega}^2 + \sum_{\substack{K_x \in \mathcal{F}_K^{\text{space}} \\ K_x \not\subset \Omega \times \{0\}}} \|\mathcal{U}^{K_x}(v)\|_{0,K_x}^2 + \|\Pi_p^* v(\cdot, T)\|_{0,\Omega}^2 \right), \end{aligned}$$

where the discrete Newton potential $\mathfrak{N}_h : \mathcal{S}_p(\mathcal{T}_h) \rightarrow Y_h$ is defined as follows: for all $v_h \in Y_h$,

$$a_h(\mathfrak{N}_h \phi_h, v_h) = c_H \left((\partial_t \phi_h, v_h)_{0,Q_T} + (\phi_h(\cdot, 0), v_h(\cdot, 0))_{0,\Omega} + \sum_{\substack{K_x \in \mathcal{F}_K^{\text{space}} \\ K_x \not\subset \Omega \times \{0\}}} (\mathcal{U}^{K_x}(\phi_h), v_h|_{K_x})_{0,K_x} \right).$$

In particular, we have the following result.

Theorem 2.1. *There exists $\gamma_I > 0$ independent of \mathcal{T}_h such that*

$$\sup_{0 \neq v_h \in Y_h} \frac{b_h(u_h, v_h)}{\|v_h\|_{Y(\mathcal{T}_h)}} \geq \gamma_I \|u_h\|_{X(\mathcal{T}_h)} \quad \forall u_h \in Y_h.$$

Therefore, method (22) is well posed.

3 Handling space–time meshes and variable degrees

We focus on the handling of the general prismatic mesh structure. More precisely, we describe refinements procedures in Section 3.1; a time-slab flagging strategy to split method (22) into smaller linear systems in Section 3.2; an element-topology flagging strategy in Section 3.3. Further, we discuss space–time virtual elements with variable degrees of accuracy in Section 3.4.

3.1 Mesh refinements

We describe a procedure to refine general prismatic space–time elements. For the sake of presentation, we consider the (1 + 1) dimensional case only; the extension to any spatial dimensions follows with a minor effort.

As discussed in Section 2.1, each mesh consists of elements with rectangular shape, with boundary given by the union of four (two space-like, two time-like) straight segments. Each straight segment may be the union of aligned edges of the element. Regardless of the number of existing hanging nodes from previous refinements, a given element K to be refined is split into four siblings by connecting the centroid of K with the midpoints of each straight segment of the boundary.

In Figure 1, we show an example of an element refinement. By this procedure, at most new five nodes are generated, fewer in presence of previously generated hanging nodes.

3.2 Time-slab flagging strategy

We present a flagging strategy that allows for the decomposition of the algebraic linear system stemming from (22) into smaller linear systems. To this aim, we assume that the first mesh of a sequence $\{\mathcal{T}_h\}$ is a “tensor-product-in-time” mesh, which can be arranged into time-slabs. On this mesh, method (22) can be assembled and solved sequentially with respect to the time-slabs.

Assume now that we are given a mesh at the refinement step $n - 1$, which is split into time-slabs. We explain here how to identify a time-slab partition of the refined mesh at step n . The time interval $[0, T]$ can be partitioned as $0 =: t_0 < \dots < t_\ell := T$, so that there exists at least one element K of the mesh at step n with K_x contained in $\Omega \times \{t_j\}$ for a $j = 0, \dots, \ell - 1$, and

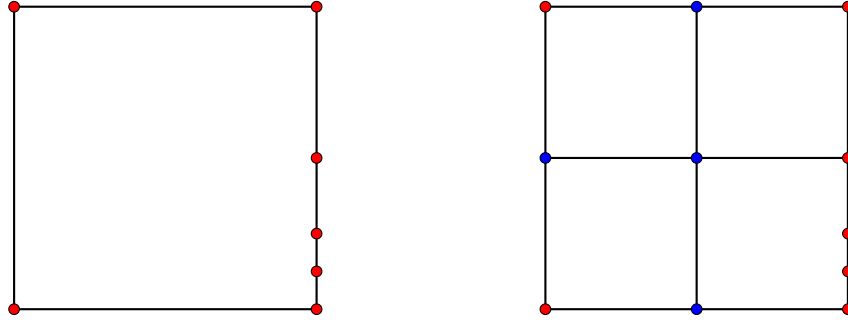


Figure 1: Element refinement strategy. We connect the centroid of the element with the midpoints of each straight segment of the boundary, regardless of the presence of previously generated hanging nodes. The red dots denote the nodes of K ; the blue dots denote the newly created nodes.

with $\mathcal{K}_t = (t_i, t_j)$ for given $i, j = 0, \dots, \ell$, $i < j$. The time-slabs may be generated cycling on the t_j , $j = 1, \dots, \ell - 1$: if all the elements in the mesh at step n are either below or above t_j , then a new time-slab is created by flagging all the elements that lie below the given t_j but have not been already allocated in a previously identified time-slab.

Based on the new flagging, at the n -th refinement step, we can assemble and solve method (22) sequentially on the newly created time-slabs. In Figure 2, we illustrate this flagging procedure with an example.

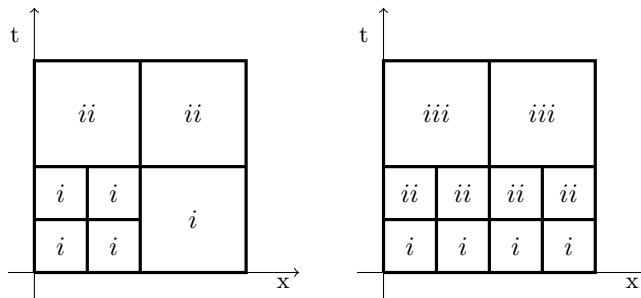


Figure 2: Left panel: we start with a given space–time mesh with prescribed time-slab structure and flagging. Right panel: time-slab flagging based on the proposed strategy after one refinement step.

3.3 Element-topology flagging strategy

A common issue in the implementation of polytopic methods is the lack of a reference element; this renders the computation of the local matrices more expensive than for methods based on simplicial or Cartesian meshes.

Assume that the elements of a given mesh \mathcal{T}_h can be grouped into a uniformly finite number of classes of equivalence (up to dilations and translations), i.e., there exists a set \mathcal{C} of “reference elements” with $\text{card}(\mathcal{C})$ uniformly bounded such that each element K of \mathcal{T}_h is equivalent to a “reference element” in \mathcal{C} . In this case, local matrices need to be computed only for the “reference elements”, thus hastening the assembling of the final system. In adaptive mesh refinements, different “reference elements” may appear. For this reason, we introduce a flag associated with the element topology that identifies the corresponding “reference element”.

For instance, in Figure 3 (left panel), we only have one “reference element” (a space–time square); in Figure 3 (central panel), we have two types of elements (a space–time square and a space–time rectangle with one hanging node on the left vertical facet); in Figure 3 (right panel), we have two types of elements (a space–time square and a space–time rectangle with one hanging node on the lower horizontal facet). Inside each element, we denote the associated “topology-flag” with a natural number.

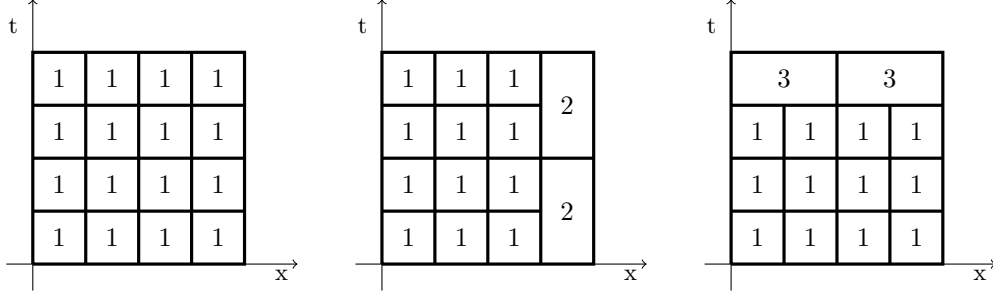


Figure 3: **Left panel:** a mesh consisting of equivalent elements. **Central panel:** a mesh with nonmatching time-like facets. **Right panel:** a mesh with nonmatching space-like facets.

In Figure 4, we present three situations that are more elaborated than those in Figure 3.

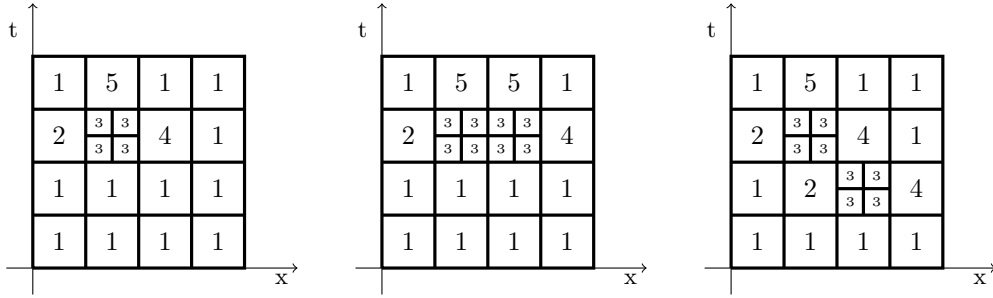


Figure 4: Three different meshes with element-topology flagging.

3.4 Space–time virtual element spaces with variable degrees of accuracy

Let \mathcal{T}_h be a given space–time polytopical mesh consisting of $N_{\mathcal{T}_h}$ elements and $\mathbf{p} \in \mathbb{N}^{N_{\mathcal{T}_h}}$ be a given distribution of degrees of accuracy. More precisely, we sort the elements of \mathcal{T}_h as $\{K_j\}_{j=1}^{N_{\mathcal{T}_h}}$, and denote the degree of accuracy in each element K_j by p_j , $j = 1, \dots, N_{\mathcal{T}_h}$.

Given the vector \mathbf{p} , we fix the degrees of freedom associated with each element according to the following maximum strategy:

- in each element K_j , $j = 1, \dots, N_{\mathcal{T}_h}$, we take bulk moments (8) up to degree $p_j - 1$;
- on each internal *time-like* facet F shared by two different elements K_j and K_ℓ for given $j, \ell = 1, \dots, N_{\mathcal{T}_h}$, we take *time-like* moments (9) up to degree $\max(p_j, p_\ell)$;
- on each boundary *time-like* facet F on the boundary of the element K_j for a given $j = 1, \dots, N_{\mathcal{T}_h}$, we take *time-like* moments (9) up to degree p_j ;
- for each K_j sharing its volume with $\mathcal{K}_j = \mathcal{K}_{\mathbf{x},j} \times \mathcal{K}_{t,j}$ for a given $j = 1, \dots, N_{\mathcal{T}_h}$, we take the *space-like* moments (10) on $\mathcal{K}_{\mathbf{x}}$ up to degree p_j .

We collect the *time-like* polynomial degrees in the vector $\mathbf{p}^{\text{time}} \in \mathbb{N}^{\text{card}(\mathcal{F}_h^{\text{time}})}$ and the *space-like* polynomial degrees in the vector $\mathbf{p}^{\text{space}} \in \mathbb{N}^{N_{\mathcal{T}_h}}$. We order the *time-like* facets in \mathcal{F}_h as $\{F_j\}_{j=1}^{\text{card}(\mathcal{F}_h^{\text{time}})}$.

Given \tilde{c}_H^K and \tilde{v}^K as in (6), the corresponding local space on the element K_j reads

$$V_h(K_j) := \left\{ v \in L^2(K_j) \mid \tilde{c}_H^K \partial_t v_h - \tilde{v}^K \Delta_{\mathbf{x}} v_h \in \mathbb{P}_{p_j-1}(K_j); v_h|_{\mathcal{K}_{\mathbf{x},j}} \in \mathbb{P}_{p_j^{\text{space}}}(\mathcal{K}_{\mathbf{x},j}); \right. \\ \left. \mathbf{n}_{F_k, \mathbf{x}} \cdot \nabla_{\mathbf{x}} v_h|_{F_k} \in \mathbb{P}_{p_k^{\text{time}}}(F_k) \forall F_k \in \mathcal{F}_{K_j}^{\text{time}} \right\}.$$

The global space Y_h is constructed by the nonconforming coupling of the *time-like* degrees of freedom (9). An immediate consequence of this maximum strategy is that $\mathbb{P}_{p_j}(K_j)$ is contained in $V_h(K_j)$.

To illustrate the maximum strategy, we provide an example in Figure 5, where we consider a uniform Cartesian mesh of 4 elements with different degrees of accuracy.

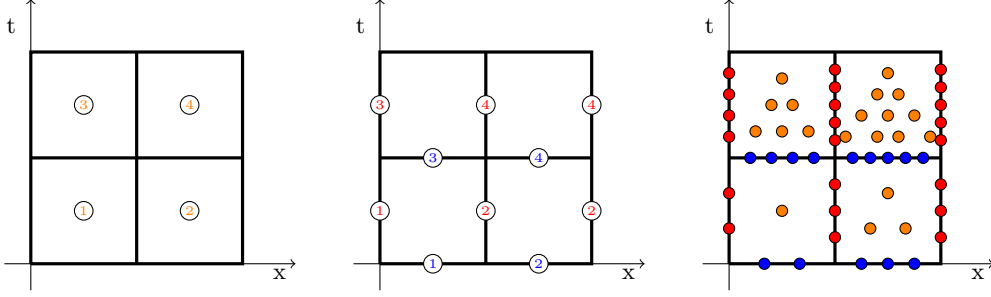


Figure 5: **Left panel:** initial distribution of degrees of accuracy over the elements. **Central panel:** “polynomial degrees” on *space-like* (blue) and *time-like* (red) facets. **Right panel:** corresponding degrees of freedom; the orange dots denote the bulk moments; the blue dots denote the *space-like* moments; the red dots denote the *time-like* moments.

4 Numerical investigation: convergence tests

We assess the convergence of the h - and hp -versions of the virtual element method (VEM) in (22). Since the virtual element solution u_h is not known in closed form and the error in the $X(\mathcal{T}_h)$ norm is not computable, we report the following error quantities: given u_h the solution to (22),

$$\begin{aligned} \mathcal{E}^Y &:= \left\| u - \Pi_p^N u_h \right\|_{Y(\mathcal{T}_h)}, & \mathcal{E}^N &:= \left\| \Pi_p^N (\mathfrak{R}_h \Pi_p^*(u - u_h)) \right\|_{Y(\mathcal{T}_h)}, \\ (\mathcal{E}^U)^2 &:= \frac{c_H}{2} \left(\left\| \Pi_p^*(u - u_h)(\cdot, 0) \right\|_{0,\Omega}^2 + \sum_{\substack{K_x \in \mathcal{F}_K^{\text{space}} \\ K_x \not\subset \Omega \times \{0\}}} \left\| \mathcal{U}^{K_x} (\Pi_p^*(u - u_h)) \right\|_{0,K_x}^2 + \left\| \Pi_p^*(u - u_h)(\cdot, T) \right\|_{0,\Omega}^2 \right), & (23) \\ (\mathcal{E}^X)^2 &:= (\mathcal{E}^Y)^2 + (\mathcal{E}^N)^2 + (\mathcal{E}^U)^2. \end{aligned}$$

4.1 Test cases

We consider test cases with coefficients $\nu = 1$ and $c_H = 1$. The right-hand side f , and the boundary and initial conditions are computed accordingly to the exact solutions below.

Test case 1. We define the analytic function

$$u_1(x, t) := \exp(-t) \sin(\pi x) \quad \forall (x, t) \in Q_T := (0, 1) \times (0, 1). \quad (24)$$

Test case 2. For $\alpha > \frac{1}{2}$, we define the function

$$u_2(x, t) := \sin(\pi x) t^\alpha \quad \forall (x, t) \in Q_T := (0, 1) \times (0, 0.1), \quad (25)$$

which belongs to $H^{\alpha+1/2-\varepsilon}(0, 1; \mathcal{C}^\infty(\Omega))$, $\varepsilon > 0$.

Test case 3. We define the function

$$u_3(x, t) := \sum_{n=0}^{\infty} \frac{4}{(2n+1)\pi} \sin((2n+1)\pi x) \exp(-(2n+1)^2 \pi^2 t) \quad \forall (x, t) \in Q_T := (0, 1) \times (0, 1), \quad (26)$$

which is the Fourier series of the solution to (3) with zero source term f , initial condition $u_0 = 1$, and homogeneous Dirichlet boundary conditions g . In the numerical experiments, the series in (25) is truncated at $n = 250$. The function u_3 belongs to $H^s(0, 1; H_0^1(0, 1))$ for any $s < 1/4$ and to $H^1(0, 1; H^{-1}(\Omega)) \cap L^2(0, 1; H_0^1(\Omega)) \setminus H^1(Q_T)$; see [16]. In particular, u_3 is singular at the interface of the (incompatible) initial and boundary conditions.

4.2 h - and hp -versions for singular solutions

The performance of the h -version of the method on smooth solutions was investigated in [10] and is therefore omitted here. The test case 1 is used in Section 5 below.

We focus on the convergence of the h - and hp -versions of the method for singular solutions. To that aim, we consider the test cases 2 and 3. Notably, we want to assess exponential convergence in terms of the cubic root of the number of degrees of freedom for the hp -version on certain geometrically refined space–time meshes.

First, we consider the test case 2. For the h -version of the method, we consider uniform degree of accuracy $p = 1$ and a sequence of uniform Cartesian space–time meshes with $h_t = 2h_x = 0.2 \times 2^{-i}$, $i = 1, \dots, 6$. For the hp -version of the method, we proceed similarly as in [4, Example 2]: we fix a partition of the spatial domain with $h_x = 0.05$ and consider a sequence of temporal meshes geometrically graded towards $t = 0$ with grading factor $\sigma_t = 0.1$. In addition, the degree of accuracy p is increased by 1 from one time slab to the next one. In Figure 6, we depict the first three meshes with varying degrees of accuracy.

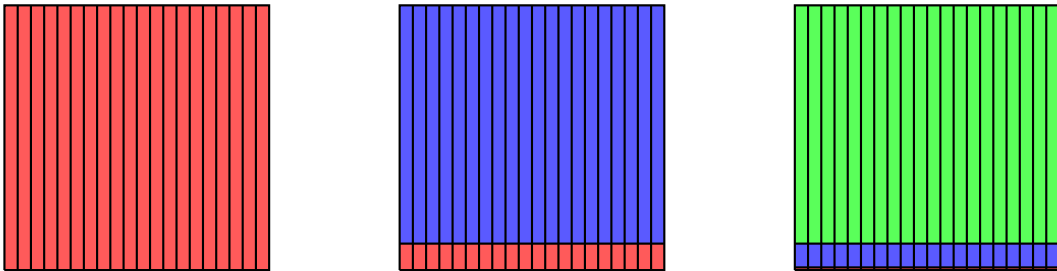


Figure 6: First three meshes employed in the hp refinements for the test case 2 with exact solution u_2 in (25). The space–time domain is $Q_T = (0, 1) \times (0, 0.1)$. For a better understanding of the figure, we scale the t -coordinates by 10. In colours, we represent the local degrees of accuracy: **red**: $p = 1$; **blue**: $p = 2$; **green**: $p = 3$.

In Figures 7 and 8, we show the errors in (23) for $\alpha = 0.55$ and $\alpha = 0.75$, respectively. Exponential convergence in terms of the cubic root of the number of degrees of freedom is observed for the hp -version of the method and both values of α . In all cases, the h -version is outperformed and displays only an algebraic decay of the error.

Next, we focus on the test case 3. For the h -version of the method, we consider uniform degree of accuracy $p = 1$, and a sequence of uniform Cartesian space–time meshes with $h_x = 0.5h_t = 2^{-i}$, $i = 1, \dots, 8$. For the hp -version of the method, we proceed similarly as in [16, Section 7.4]: we consider a sequence of space–time meshes geometrically graded towards $x = 0$, $x = 1$ and $t = 0$ with grading factors $\sigma_x = \sigma_t = 0.25$. In Figure 9, we depict the first three meshes with varying degrees of accuracy.

In Figure 10, we show the errors in (23). Exponential convergence in terms of the cubic root of the number of degrees of freedom is observed for the hp -version of the method; only algebraic convergence is observed for the h -version.

5 Numerical investigation: an adaptive procedure

We consider a standard adaptive algorithm of the form

$$\mathbf{SOLVE} \implies \mathbf{ESTIMATE} \implies \mathbf{MARK} \implies \mathbf{REFINE}. \quad (27)$$

We base the **MARK** step on a Dörfler marking strategy with parameter θ that we shall specify at each occurrence. The **REFINE** step involves only space–time mesh element refinements as described in Section 3.1. For the **ESTIMATE** step, we use the following local, computable residual-type error indicator: given an element $K \in \mathcal{T}_h$,

$$\eta_K^2 := \sum_{i=1}^5 \eta_{K,i}^2,$$

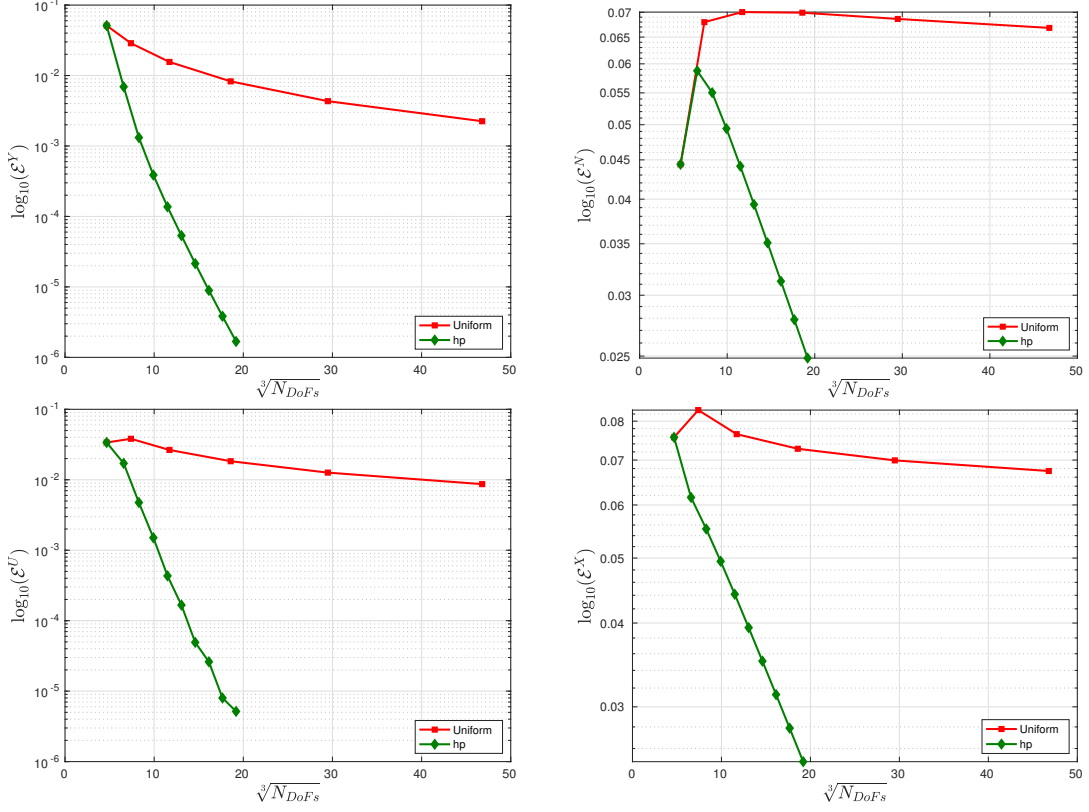


Figure 7: Convergence of the errors in (23) for the h - and hp -versions of the method. We consider the test case 2 with exact solution u_2 in (25), $\alpha = 0.55$.

where

$$\begin{aligned}
\eta_{K,1}^2 &:= \nu^{-1} \frac{h_{K_x}^2}{p^2} \|f + \nu \Delta_x \Pi_p^N u_h - c_H \partial_t \Pi_p^* u_h\|_{0,K}^2, \\
\eta_{K,2}^2 &:= \frac{1}{2} \nu^{-1} \sum_{\substack{F \in \mathcal{F}_K^{\text{time}}, \\ F \not\subset \partial\Omega \times (0,T)}} \frac{h_{F_x}}{p} \|\nu [\nabla_x \Pi_p^N u_h]\|_{0,F}^2, \\
\eta_{K,3}^2 &:= \nu \sum_{\substack{F \in \mathcal{F}_K^{\text{time}}, \\ F \subset \partial\Omega \times (0,T)}} p h_{F_x}^{-1} \|\Pi_p^N u_h\|_{0,F}^2 + \frac{1}{2} \nu \sum_{\substack{F \in \mathcal{F}_K^{\text{time}}, \\ F \not\subset \partial\Omega \times (0,T)}} p h_{F_x}^{-1} \|[\Pi_p^N u_h]\|_{0,F}^2, \\
\eta_{K,4}^2 &:= \sum_{K_x \in \mathcal{F}_K^{\text{space}}} c_H^{-1} \|\mathcal{U}^{K_x}(u_h)\|_{0,K_x}^2, \\
\eta_{K,5}^2 &:= \nu S^K ((I - \Pi_p^N)u_h, (I - \Pi_p^N)u_h).
\end{aligned} \tag{28}$$

The above local residual-type error indicator consists of five terms: $\eta_{K,1}$ is the internal residual of the projected discrete solution; $\eta_{K,2}$ is the boundary residual involving the normal trace of the gradient of the projected discrete solution; $\eta_{K,3}$ is a term due to the nonconformity in space involving the jump of traces on time-like facets; $\eta_{K,4}$ is related to the upwind terms in the scheme; $\eta_{K,5}$ is a correction term due to the virtual element stabilization of the method.

The global error indicator and its parts read

$$\eta^2 := \sum_{i=1}^5 \eta_i^2, \quad \eta_i^2 := \sum_{K \in \mathcal{T}_h} \eta_{K,i}^2. \tag{29}$$

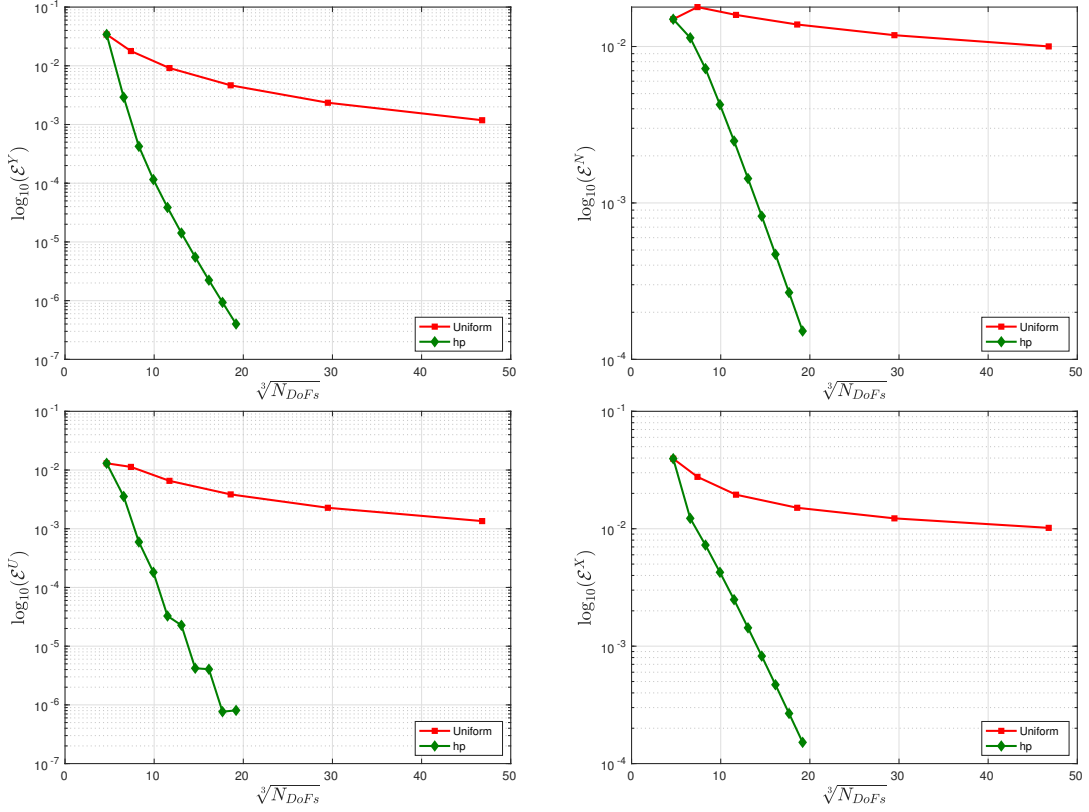


Figure 8: Convergence of the errors in (23) for the h - and hp -versions of the method. We consider the test case 2 with exact solution u_2 in (25), $\alpha = 0.75$.

5.1 Assessment of the reliability and efficiency of the error indicator

We test the performance of the proposed error indicator η in (29). To this aim, we introduce the effectivity index related to the computable error \mathcal{E}^Y :

$$\text{effectivity index} := \frac{\eta}{\mathcal{E}^Y}. \quad (30)$$

In Figure 11 (left panel), we assess numerically the reliability and efficiency of η for the test case 1 with exact solution u_1 in (24) under uniform mesh refinements, starting from a uniform space–time Cartesian mesh with $h_x = h_t = 0.1$. The effectivity indices for $p = 1, 2, 3$, tend to constant values, whence the error indicator η appears to be efficient and reliable with respect to the error \mathcal{E}^Y .

In Figure 11 (right panel), we show all the errors in (23) and the five terms appearing in the error indicator (29) for degree of accuracy $p = 1$. The error indicator η decays with order $\mathcal{O}(N_{DoFs}^{-\frac{1}{2}})$, i.e., slower than that for the error \mathcal{E}^N in (23), which decays with order $\mathcal{O}(N_{DoFs}^{-1})$. This suggests that the error indicator η is not efficient with respect to the error \mathcal{E}^N .

Next, we focus on the test cases 2 and 3 with singular solutions u_2 ($\alpha = 0.55$ and 0.75) in (25) and u_3 in (26) on the space–time domains $Q_T = (0, 1) \times (0, 1)$ and $Q_T = (0, 1) \times (0, 0.1)$, respectively. In Figures 12–14, we show the decay of the errors in (23) and of the five terms appearing in the error indicator under uniform mesh refinements, starting with Cartesian meshes with $h_x = 10h_t = 0.1$ (for the test case 2) and $h_x = h_t = 0.1$ (for the test case 3). In all cases, the effectivity indices shown on the left panels tend to constant values, which suggests that the error indicator (29) is efficient and reliable with respect to the error \mathcal{E}^Y also for singular solutions.

For the test case 2, the errors \mathcal{E}^Y and \mathcal{E}^N decay with orders $\mathcal{O}(N_{DoFs}^{-\frac{1}{2}(\alpha+\frac{1}{2})})$ and $\mathcal{O}(N_{DoFs}^{-\frac{1}{2}(\alpha-\frac{1}{2})})$, respectively; see Figures 12 and 13. The error indicator η decays with the same order as that of the error \mathcal{E}^Y , while it is not reliable with respect to the error \mathcal{E}^N .

For the test case 3, the error indicator η and all the errors in (23) decay with the same order, namely $\mathcal{O}(N_{DoFs}^{-\frac{1}{8}})$; see Figure 14.

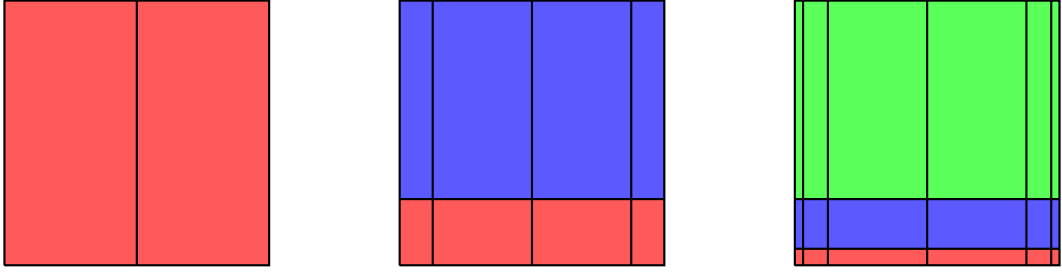


Figure 9: First three meshes employed in the hp refinements for the test case 2 with exact solution u_2 in (25). The space-time domain is $Q_T = (0, 1) \times (0, 1)$. In colours, we represent the local degrees of accuracy: **red:** $p = 1$; **blue:** $p = 2$; **green:** $p = 3$.

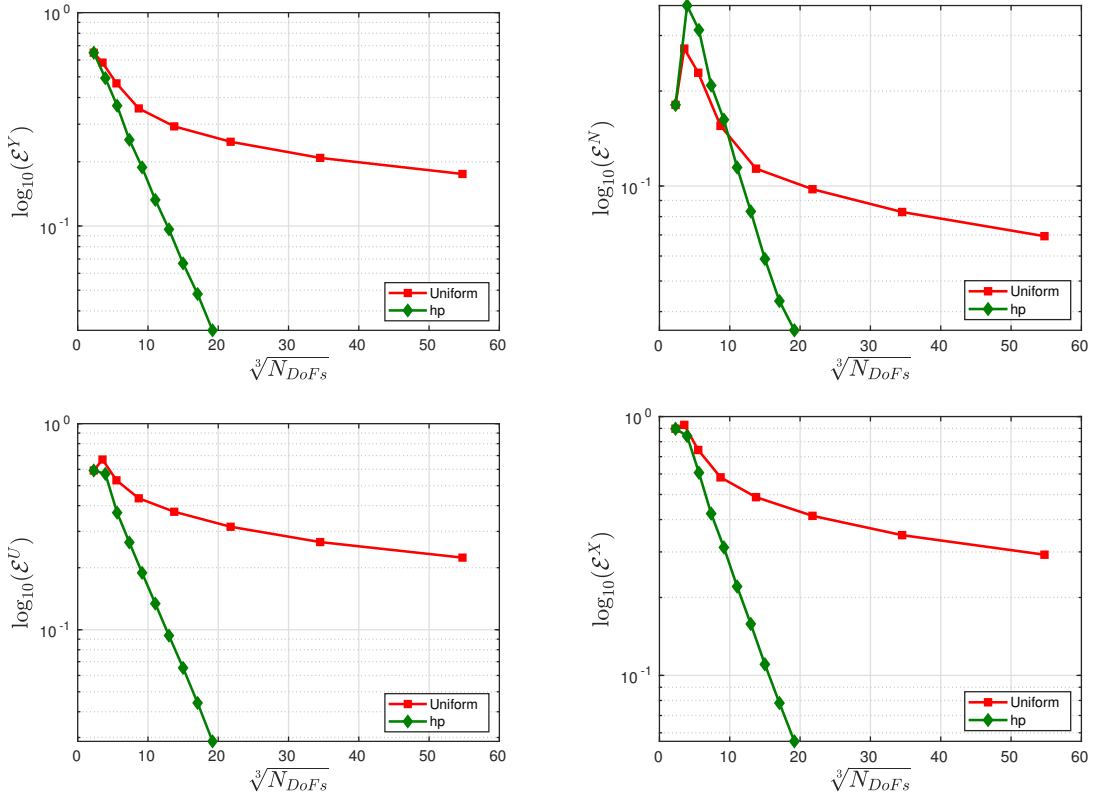


Figure 10: Convergence of the errors in (23) for the h - and hp -versions of the method. We consider the test case 3 with exact solution u_3 in (26).

In summary, the above experiments seem to indicate that the error indicator η is reliable and efficient for the error \mathcal{E}^Y but not for the error \mathcal{E}^N .

5.2 Adaptive mesh refinements

We test the performance of method (22) under adaptive mesh refinements as described in (27). We consider the test cases 2 and 3 with exact solutions u_2 ($\alpha = 0.55$) in (25) and u_3 in (26), respectively. The marking step is dictated by the error indicator in (29).

We are also interested in comparing the results with those obtained with an adaptive procedure for the continuous finite element method (FEM) of (5) in [18]:

$$\begin{cases} \text{find } \tilde{u}_h \in \tilde{X}_h \text{ such that} \\ b(\tilde{u}_h, \tilde{v}_h) = (f, \tilde{v}_h)_{0, Q_T} \quad \forall \tilde{v}_h \in \tilde{Y}_h. \end{cases} \quad (31)$$

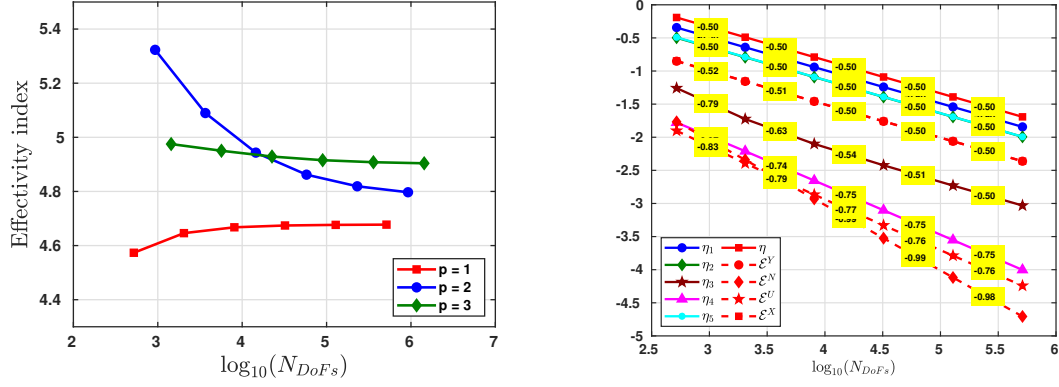


Figure 11: The test case 1 with exact solution u_1 in (24). **Left panel:** Effectivity index. **Right panel:** Comparison of the errors in (23) with the terms appearing in the error indicator (29) for $p = 1$.

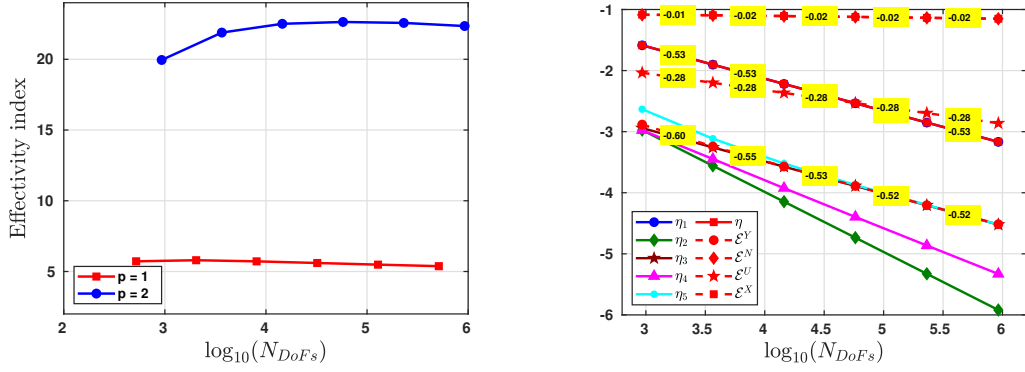


Figure 12: The test case 2 with exact solution u_2 in (25) and $\alpha = 0.55$. **Left panel:** Effectivity index. **Right panel:** Comparison of the errors in (23) with the terms appearing in the error indicator (29) for $p = 2$.

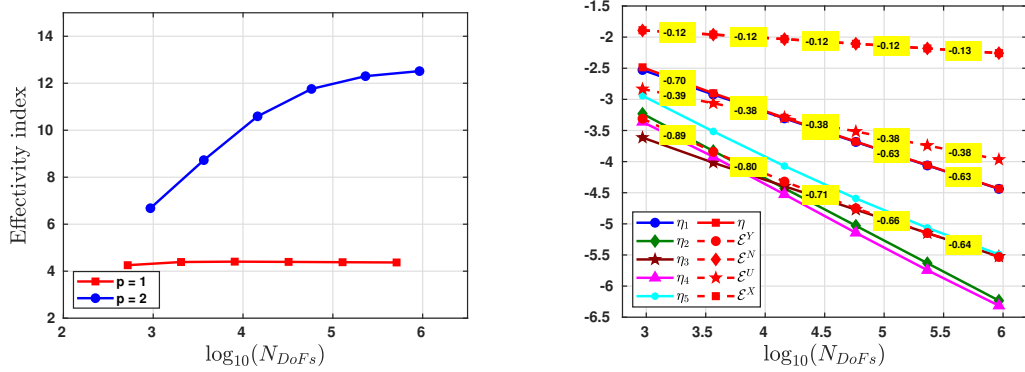


Figure 13: The test case 2 with exact solution u_2 in (25) and $\alpha = 0.75$. **Left panel:** Effectivity index. **Right panel:** Comparison of the errors in (23) with the terms appearing in the error indicator (29) for $p = 2$.

Above, \tilde{Y}_h is a space of continuous piecewise polynomials over a space-time simplicial tessellation of Q_T and \tilde{X}_h is the subspace of \tilde{Y}_h of functions with zero initial condition. We recall the residual-

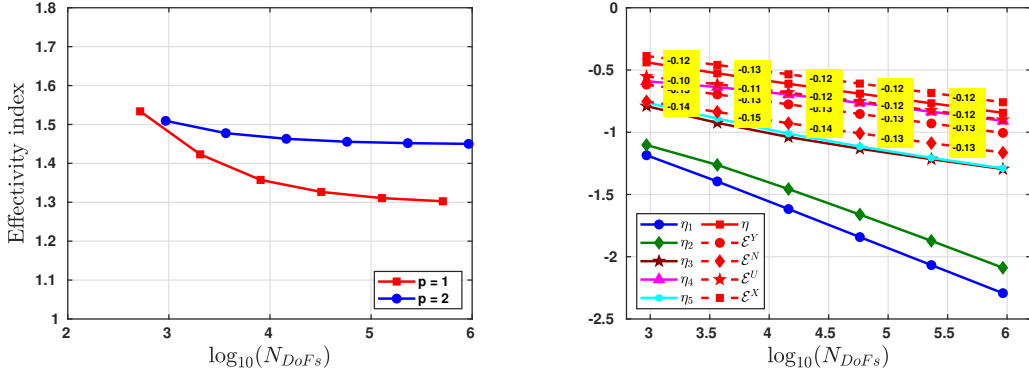


Figure 14: The test case 3 with exact solution u_3 in (26). **Left panel:** Effectivity index. **Right panel:** Comparison of the errors in (23) with the terms appearing in the error indicator (29) for $p = 2$.

type error indicator introduced in [19, 20]:

$$\begin{aligned} \tilde{\eta}^2 &:= \sum_{i=1}^2 \tilde{\eta}_i^2, & \tilde{\eta}_i^2 &:= \sum_{K \in \mathcal{T}_h} \tilde{\eta}_{K,i}^2, \\ \tilde{\eta}_{K,1}^2 &:= \frac{h_K^2}{p^2} \|f + \nu \Delta_{\mathbf{x}} \tilde{u}_h - c_H \partial_t \tilde{u}_h\|_{0,K}^2, & \tilde{\eta}_{K,2}^2 &:= \frac{1}{2} \sum_{F \in \mathcal{F}_K^{\text{time}}} \frac{h_F}{p} \|\nu [\nabla_{\mathbf{x}} \tilde{u}_h]\|_{0,F}^2, \end{aligned} \quad (32)$$

and the error quantity

$$E^Y = \|u - \tilde{u}_h\|_Y. \quad (33)$$

For the VEM, we start with a mesh with 1 element; for the continuous FEM, we start with a structured simplicial mesh with 2 elements.

In Figure 15, we show the errors of both methods under uniform and adaptive mesh refinements for the test case 2 with $\alpha = 0.55$. Uniform and adaptive mesh refinements for the VEM in (22) lead to higher convergence rates than those for the continuous FEM in (31). For the Dörfler marking strategy, we set $\theta = 0.99$ for the VEM and $\theta = 0.9$ for the FEM.

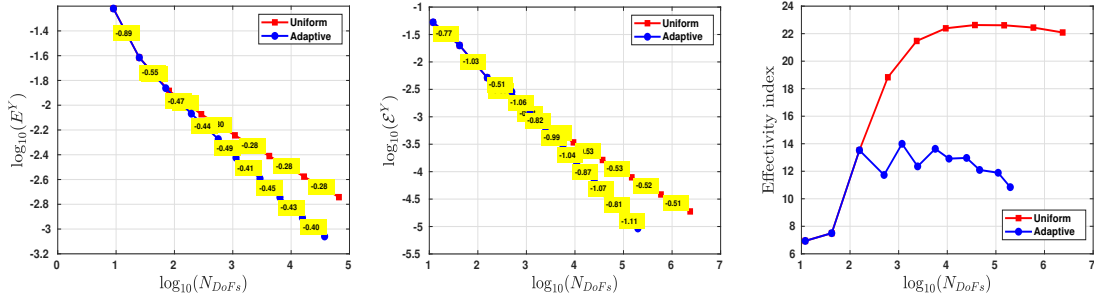


Figure 15: The test case 2 with exact solution u_2 in (25) and $\alpha = 0.55$. **Left panel:** Error E^Y for the continuous FEM with $p = 2$ under uniform and adaptive mesh refinements, with convergence rates of approximately $\mathcal{O}(N_{Dof_s}^{-0.28})$ and $\mathcal{O}(N_{Dof_s}^{-0.40})$, respectively. **Central panel:** Error E^Y for the VEM with $p = 2$ under uniform and adaptive mesh refinements, with convergence rates of approximately $\mathcal{O}(N_{Dof_s}^{-0.52})$ and $\mathcal{O}(N_{Dof_s}^{-1})$, respectively. **Right panel:** The effectivity index for the adaptive VEM.

In Figure 16, we show the Y -type errors for both methods under uniform and adaptive mesh refinements with Dörfler marking parameter $\theta = 0.9$ for the test case 3 and $p = 1$. The adaptive procedure for the VEM (22) leads to higher convergence rates compared to those obtained for uniform refinements. For the continuous FEM (31), although the adaptive procedure produces meshes that are refined towards the bottom corners as in Figure 18 (right panels), the error E^Y does not converge to zero.

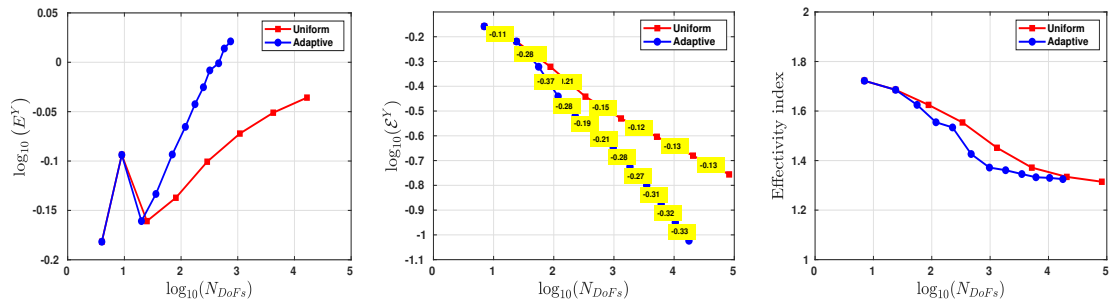


Figure 16: The test case 3 with exact solution u_3 in (26). **Left panel:** Error E^Y for the continuous finite element with $p = 1$ under uniform and adaptive refinements. **Central panel:** Error \mathcal{E}^Y for the VEM with $p = 1$ under uniform and adaptive mesh refinements, with convergence rates of approximately $\mathcal{O}(N_{Dof_s}^{-0.13})$ and $\mathcal{O}(N_{Dof_s}^{-3.3})$, respectively. **Right panel:** The effectivity index for the adaptive VEM.

In Figures 17 and 18, we plot some meshes for the test cases with exact solutions u_2 ($\alpha = 0.55$) and u_3 , respectively, produced by the adaptive procedure driven by the VEM error indicator in (29) and the continuous FEM error indicator in (32).

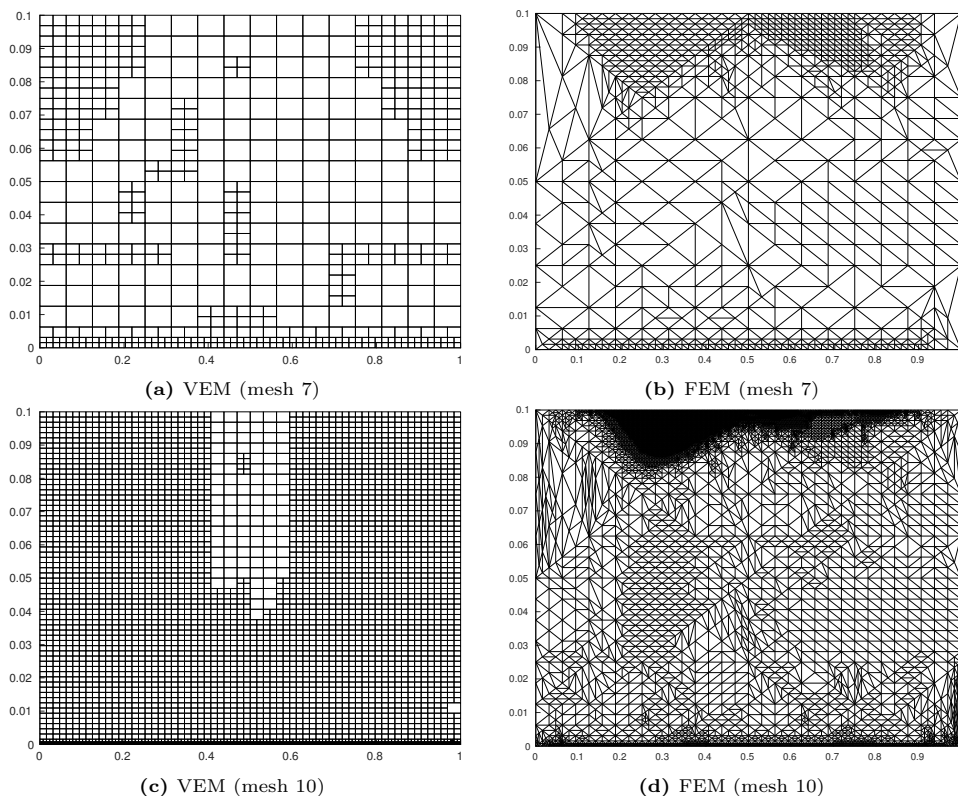


Figure 17: Meshes generated by the adaptive schemes driven by the VEM error indicator η in (29) (left panel) and the continuous FEM error indicator $\tilde{\eta}$ (right panel) for the test case with exact solutions u_2 ($\alpha = 0.55$) in (25).

Next, in Tables 1 and 2, we focus on the adaptive mesh refinements driven by the VEM error indicator in (29) and report the number of time-slabs and “reference elements” as in Sections 3.2 and 3.3 for some adaptively generated meshes;. The time-slab and the element-topology strategies allow us to hasten considerably the assembling and the solving time of method (22).

6 Conclusions

We extended the virtual element framework of [10] to the case of general prismatic space-time meshes with possible hanging nodes and nonuniform degrees of accuracy, useful in hp -adaptive

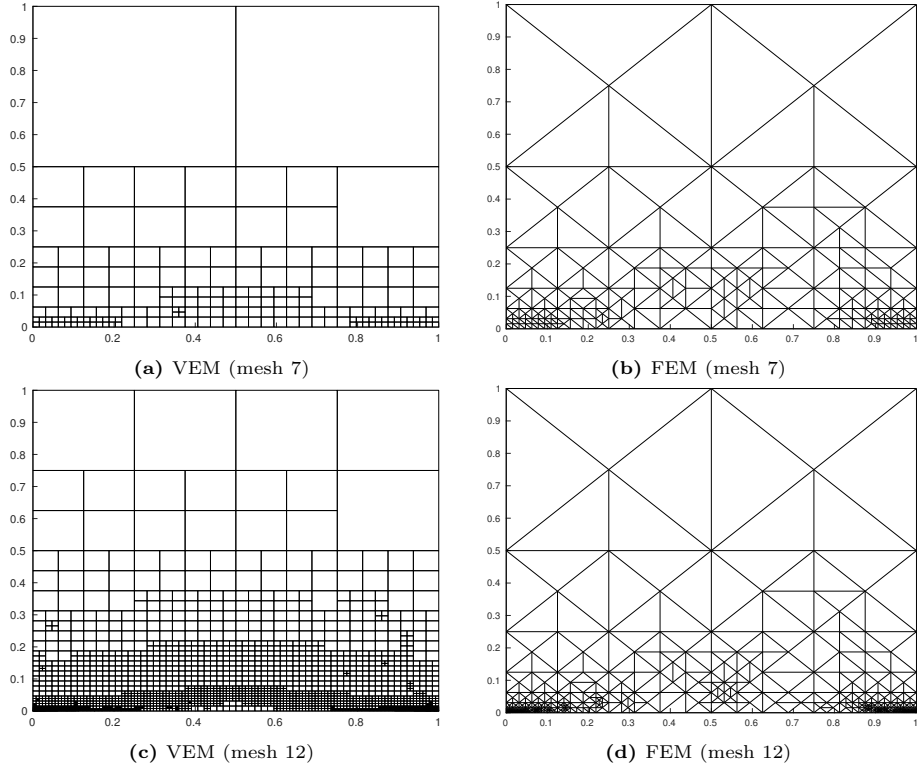


Figure 18: Meshes generated by the adaptive schemes driven by the VEM error indicator η in (29) (left panel) and the continuous FEM error indicator $\tilde{\eta}$ in (32) (right panel) for the test case with exact solutions u_3 in (26).

Table 1 Performance of flagging strategies for the test case 2 with $\alpha = 0.55$, $p = 2$ and adaptive refinements.

Mesh	Number of reference elements	Total number of elements	Number of time-slabs
m_2	1	4	2
m_4	1	52	5
m_6	16	265	10
m_8	19	1189	21
m_{10}	24	5110	45
m_{12}	24	21883	103

Table 2 Performance of flagging strategies for the test case 3 with $p = 1$ and adaptive refinements.

Mesh	Number of reference elements	Total number of elements	Number of time-slabs
m_2	1	4	2
m_4	3	22	4
m_6	9	91	5
m_8	21	361	9
m_{10}	33	1204	13
m_{12}	35	3493	21

procedures. We discussed flagging strategies to handle the space-time meshes data structure; this improves the performance of the method. We investigated numerically the hp -version of the method and demonstrated the expected exponential convergence in terms of suitable roots of the number of degrees of freedom for singular solutions. A residual-type error indicator was introduced and an h -adaptive refinement procedure was tested based on it. This error indicator appears to be reliable and efficient for the error \mathcal{E}^Y but not for the error \mathcal{E}^N in (23). We investigated numerically the overall virtual element adaptive procedure. The results obtained for certain singular solutions show that it outperforms a corresponding one for a continuous finite element method.

References

- [1] A. Aziz and P. Monk. Continuous finite elements in space and time for the heat equation. 52(186):255–274, 1989.
- [2] I. Babuška and T. Janik. The h - p version of the finite element method for parabolic equations. Part I. The p -version in time. *Numer. Methods Partial Differential Equations*, 5(4):363–399, 1989.
- [3] I. Babuška and T. Janik. The h - p version of the finite element method for parabolic equations. Part II. The h - p version in time. *Numer. Methods Partial Differential Equations*, 6(4):343–369, 1990.
- [4] A. Cangiani, Z. Dong, and E.H. Georgoulis. hp -version space-time discontinuous Galerkin methods for parabolic problems on prismatic meshes. *SIAM J. Sci. Comput.*, 39(4):A1251–A1279, 2017.
- [5] R. Dautray and J.-L. Lions. *Mathematical Analysis and Numerical Methods for Science and Technology, volume 5, Evolution Problems I*. Springer-Verlag, 1992.
- [6] K. Eriksson, C. Johnson, and V. Thomée. Time discretization of parabolic problems by the discontinuous Galerkin method. *ESAIM Math. Model. Numer. Anal.*, 19(4):611–643, 1985.
- [7] D. French and T. Peterson. A continuous space-time finite element method for the wave equation. *Math. Comp.*, 65(214):491–506, 1996.
- [8] T. Führer and M. Karkulik. Space–time least-squares finite elements for parabolic equations. *Comput. Math. Appl.*, 92:27–36, 2021.
- [9] G. Gantner and R. Stevenson. Further results on a space-time FOSLS formulation of parabolic PDEs. *ESAIM Math. Model. Numer. Anal.*, 55(1):283–299, 2021.
- [10] S. Gómez, L. Mascotto, A. Moiola, and I. Perugia. Space-time virtual elements for the heat equation. <https://arxiv.org/abs/2212.05343>, 2022.
- [11] T. J. R. Hughes and J. R. Stewart. A space-time formulation for multiscale phenomena. *J. Comput. Appl. Math.*, 74(1-2):217–229, 1996.
- [12] P. Jamet. Galerkin-type approximations which are discontinuous in time for parabolic equations in a variable domain. *SIAM J. Numer. Anal.*, 15(5):912–928, 1978.
- [13] U. Langer, S. E. Moore, and M. Neumüller. Space–time isogeometric analysis of parabolic evolution problems. *Comput. Methods Appl. Mech. Engrg.*, 306:342–363, 2016.
- [14] M. Montardini, M. Negri, G. Sangalli, and M. Tani. Space–time least–squares isogeometric method and efficient solver for parabolic problems. *Math. Comp.*, 89(323):1193–1227, 2020.
- [15] A. Schafelner and P. S. Vassilevski. Numerical results for adaptive (negative norm) constrained first order system least squares formulations. *Comput. Math. Appl.*, 95:256–270, 2021.
- [16] D. Schötzau and C. Schwab. Time discretization of parabolic problems by the hp -version of the discontinuous Galerkin finite element method. *SIAM J. Numer. Anal.*, 38(3):837–875, 2000.
- [17] Ch. Schwab and R. Stevenson. Space-time adaptive wavelet methods for parabolic evolution problems. *Math. Comp.*, 78(267):1293–1318, 2009.
- [18] O. Steinbach. Space-time finite element methods for parabolic problems. *Comput. Methods Appl. Math.*, 15(4):551–566, 2015.
- [19] O. Steinbach and H. Yang. Comparison of algebraic multigrid methods for an adaptive space–time finite-element discretization of the heat equation in 3D and 4D. *Numer. Linear Algebra Appl.*, 25(3):e2143, 2018.
- [20] O. Steinbach and H. Yang. Space-time finite element methods for parabolic evolution equations: discretization, a posteriori error estimation, adaptivity and solution. *Space-Time Methods: Application to Partial Differential Equations*, 25:207–248, 2019.
- [21] O. Steinbach and M. Zank. Coercive space-time finite element methods for initial boundary value problems. *Electron. Trans. Numer. Anal.*, 52:154–194, 2020.
- [22] R. Stevenson and J. Westerdiep. Stability of Galerkin discretizations of a mixed space–time variational formulation of parabolic evolution equations. *IMA J. Numer. Anal.*, 41(1):28–47, 2021.
- [23] J.J. Sudirham, J.J.W. Van der Vegt, and R.M.J. Van Damme. Space-time discontinuous Galerkin method for advection-diffusion problems on time-dependent domains. *Appl. Numer. Math.*, 56(12):1491–1518, 2006.
- [24] K. Voronin, C. S. Lee, M. Neumüller, P. Sepulveda, and P. S. Vassilevski. Space-time discretizations using constrained first-order system least squares (CFOSLS). *J. Comput. Phys.*, 373:863–876, 2018.